

Refined RBF-FD analysis of non-Newtonian natural convection

Miha Rot^{a,b,*}, Gregor Kosec^a

^a*Jožef Stefan Institute, Jamova cesta 39, 1000 Ljubljana, Slovenia*

^b*Jožef Stefan International Postgraduate School, Jamova cesta 39, 1000 Ljubljana, Slovenia*

Abstract

In this paper we present a refined RBF-FD solution for a non-Newtonian fluid in a closed differentially heated cavity. The problem at hand is governed by three coupled nonlinear partial differential equations, namely heat transport, momentum transport and mass continuity. The non-Newtonian behaviour is modelled with the Ostwald-de Weele power law and the buoyancy with the Boussinesq approximation. The problem domain is discretised with scattered nodes without any requirement for a topological relation between them. This allows a trivial generalisation of the solution procedure to complex irregular 3D domains, which is also demonstrated by solving the problem in a 2D and 3D geometry mimicking the porous filter. The results in 2D are compared with two reference solutions that use the Finite volume method in a conjunction with two different stabilisation techniques (upwind and QUICK), where we achieved good agreement with the reference data. The refinement is implemented on top of a dedicated meshless node positioning algorithm using piecewise linear node density function that ensures sufficient node density in the centre of the domain while maximising the node density in a boundary layer where the most intense dynamic is expected. The results show that with a refined approach, up to 5 times fewer nodes are needed to obtain the results with the same accuracy compared to the regular discretisation. The paper also discusses the convergence for different scenarios for up to $2 \cdot 10^5$ nodes, the behaviour of the flow in the boundary layer, the behaviour of the viscosity and the geometric flexibility of the proposed solution procedure.

Keywords: meshless method, dimension independent, refined discretisation, Navier-Stokes, non-Newtonian fluid, power-law fluid, natural convection, heat transport

^{*}Corresponding author

Email addresses: miha.rot@ijs.si (Miha Rot), gregor.kosec@ijs.si (Gregor Kosec)

1. Introduction

Natural convection, a type of flow driven by the temperature-dependent density of a fluid, is a cornerstone of many natural and industrial processes. The most vivid examples in nature where it plays a crucial role are probably weather systems, e.g. sea and land breezes. In industry, it is of paramount importance in metal casting, various heating systems, food processing, etc [1]. The minimal model describing natural convection involves coupled heat transfer and fluid dynamics [2], where simple fluids such as air and water are usually modelled as Newtonian fluids, i.e. the viscosity of the fluid is constant. However, such an approximation becomes insufficient when dealing with more complex fluids [3] like melts of large and complicated molecules, polymers [4], suspensions, foams, biological fluids such as blood [5], food [6, 7], etc. In such fluids, also called non-Newtonian fluids, the relationship between stress and strain is no longer linear and the viscous stress becomes related to the shear rate [8]. The behaviour of non-Newtonian fluids can generally be divided into two groups, namely shear-thinning behaviour, where viscosity decreases under shear stress, and shear-thickening behaviour, where viscosity increases with the rate of shear stress. In addition, some non-Newtonian fluids exhibit a threshold value for yield stress at which the transition from solid to liquid behaviour occurs.

Because of its importance in industry and in understanding nature, the study of non-Newtonian natural convection (NNC) has attracted much research attention. Since closed-form solutions are rare and limited to extreme simplifications, the problem is usually treated numerically [9]. The dynamics of non-Newtonian fluids have been studied in various fields, from non-Newtonian blood flow in arteries [10] to injection moulding of plastics [4]. In particular, natural convection in cavities has been thoroughly analysed due to its direct application in industry [9].

From the numerical analysis point of view, the most commonly reported approaches to solving NNC in cavities are based on the finite volume method (FVM) for the discretisation of the relevant partial differential operators and Semi-Implicit Method for Pressure-Linked Equations (SIMPLE) for pressure-velocity coupling [11]. A comprehensive study of NNC solved with FVM and Quadratic Upstream Interpolation for Convective Kinematics (QUICK) to treat the convective terms was presented in [12], and with upwind stabilisation of convective terms in [13]. The FVM with QUICK was further investigated in [14] in solving NNC with internal rotating heater and cooler. Moraga et al. [15] demonstrated the multigrid FVM with a fifth power differentiation scheme for convective transport in the solution of NNC with phase change. A similar numerical approach was also used in the solution of NNC in 3D [16]. In conjunction with the Finite Difference Method (FDM) and upwind stabilisation, the solution of NNC with internal heat source was recently demonstrated in [17]. The NNC was also solved with a Finite Elements Method (FEM) [18, 19] as well as with the Lattice Boltzmann Method (LBM) [20].

All the aforementioned solution methods are mesh-based, i.e., the nodes are structured into polygons that completely cover the computational domain, a

process also known as meshing. In FDM, FVM and LBM, a regular grid is often used, making meshing a trivial task, but at the cost of complications with irregular geometries and potential refinement. At FEM, meshing is mandatory and often also the most time-consuming part of the entire solution process, especially for realistic 3D geometries, which generally cannot be automatically meshed and therefore often require the user's help. An alternative to the mesh-based methods is the meshless approach [21]. The conceptual difference between mesh-based and meshless methods is that in the latter all relationships between nodes are defined solely by internodal distances. An important implication of this distinction is that the meshless methods can work with scattered nodes, which greatly facilitates the consideration of complex 3D geometries and adaptivity.

In this paper, we introduce a novel refined Radial Basis Function Generated Finite Difference (RBF-FD) [22] meshless solution of NNC in 2D and 3D irregular domains computed on automatically generated scattered nodes [23], using the Chorin's projection method for the pressure-velocity coupling [24], and explicit time stepping. No stabilisation of the convective terms is used to minimise the impact of numerical diffusion in the results. We present a unified NNC solution procedure for 2D and 3D that can be easily extended to arbitrary geometries and inherently supports hp -adaptivity [25, 26].

Results for a reference 2D case are compared with data from Turan et al. [13] and Kim et al. [12], showing that our results are in the range of the comparative data. Therefore, in addition to a novel solution procedure, we also extend the range of available numerical solutions for the given problem with a completely different numerical approach. Note that the reference solutions differ only in the stabilisation of the convective terms (Upwind vs QUICK), otherwise in both papers results are computed with FVM and SIMPLE coupling.

The code for the presented numerical methodology and the comparison data are available at [27].

In section 2 a mathematical model of NCC is discussed, followed by a presentation of the meshless numerical method and solution procedure in section 3. The analysis of results for the reference 2D case and a showcase of the method's versatility on more complex cases are shown in sections 4 and 5.

2. Problem formulation

The dynamics of natural convection in non-Newtonian fluids are governed by a system of three partial differential equations describing the continuity of

mass, the conservation of momentum, and the transport of heat

$$\nabla \cdot \mathbf{v} = 0, \quad (1)$$

$$\rho \left(\frac{\partial \mathbf{v}}{\partial t} + \mathbf{v} \cdot \nabla \mathbf{v} \right) = -\nabla p + \nabla \cdot (\eta \nabla \mathbf{v}) - \mathbf{g} \rho \beta T_\Delta, \quad (2)$$

$$\rho c_p \left(\frac{\partial T}{\partial t} + \mathbf{v} \cdot \nabla T \right) = \nabla \cdot (\lambda \nabla T), \quad (3)$$

$$\eta = \eta_0 \left(\frac{1}{2} \left\| \nabla \mathbf{v} + (\nabla \mathbf{v})^T \right\| \right)^{\frac{n-1}{2}}, \quad (4)$$

with \mathbf{v} , T , p , ρ , \mathbf{g} , β , T_Δ , c_p , η_0 , n , representing the flow velocity field, temperature field, pressure field, density, gravity, thermal expansion coefficient, temperature offset, heat capacity, viscosity constant and non-Newtonian exponent, respectively.

The buoyancy force that drives the natural convection dynamics is relatively weak and ensures that the maximum velocity remains well below the speed of sound. This allows us to model the fluid as incompressible [28] and reduce the continuity equation to (1). The fluid motion is described by the Navier-Stokes equation (2), which is modified from its usual form by the addition of a force term describing the buoyancy caused by the thermal expansion. This force is approximated by the Boussinesq approximation [29], which is based on the assumption that the acceleration of a fluid driven by natural convection remains insignificant compared to gravity and consequently the small thermal fluctuations of the density only play a role when amplified by the strong gravity in the buoyancy term. The Boussinesq approximation couples the fluid motion described by the Navier-Stokes equation (2) with the temperature described by the heat transfer equation (3) and thus establishes the model for natural convection driven by the presence of a temperature gradient.

The normally constant viscosity η is replaced by the Ostwald-de Waele power law model [9] defined with equation 4. The shear dependence is captured by the exponentiated tensor norm of the shear rate tensor ¹ and controlled by the exponent n , which controls the extent of the non-Newtonian behaviour, and η_0 , which is used as a scaling factor.

The model reduces to a Newtonian fluid when $n = 1$ and can be used to describe both shear thickening behaviour with $n > 1$ and shear thinning behaviour with $n < 1$. We focus on the latter as it leads to stronger convection, i.e. more interesting flow behaviour, and is more common in realistic fluids. A visualisation of the viscosity dependence for an arbitrarily chosen range of shear rate norms can be found on the right-hand panel of Figure 1 for a range of exponents that we will use in further analysis. It can be seen from the figure that while n has a dramatic impact on the effective viscosity, there is also a problem with the divergent viscosity at low shear rates in the shear thinning regime.

¹The shear rate tensor for incompressible fluids is the same as the strain rate tensor, which can be expressed as the symmetric part of the velocity gradient.

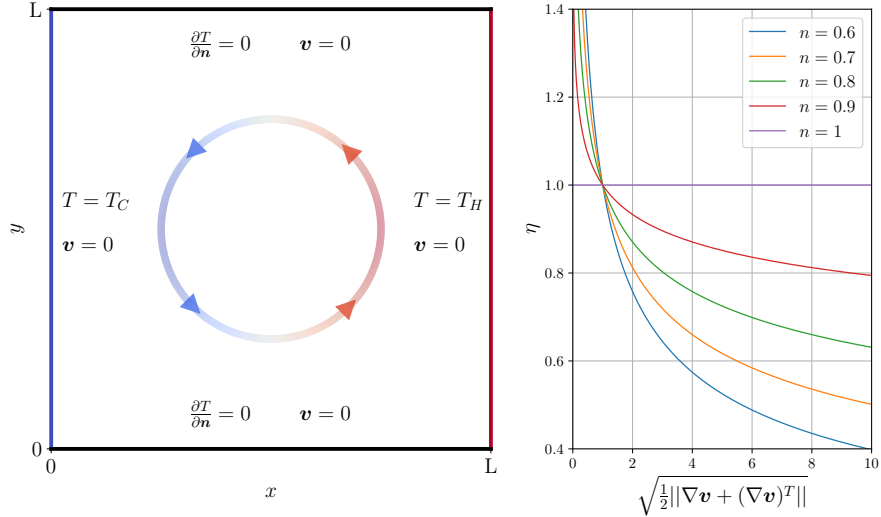


Figure 1: *left*: A schematic representation of the De Vahl Davis differentially heated cavity case with velocity and temperature boundary conditions. *right*: Relationship between viscosity and shear rate for a $n = 1$ Newtonian and a selection of shear-thinning $n < 1$ non-Newtonian cases.

This is mainly a problem for the initial, transient part of the simulation, where a flow pattern emerges from the initially stationary fluid and can be solved by downward bounding² the shear rate norm used in the power law to 10^{-10} .

Model parameters that reflect the behaviour of a realistic fluid can be determined by fitting the model to experimental data. Unfortunately, because the model represents the simplest approach to describing shear-dependent behaviour, it is only suitable for the intermediate shear rate regime and must be extended to accurately represent the asymptotic behaviour exhibited by realistic shear-thinning fluids at low and high shear rates. The plethora of resulting specialised models are more complex in the sense that they have more parameters and a more convoluted algebraic form. However, from a numerical point of view, the more complex models do not affect the solution procedure and do not introduce additional numerical problems.

The natural convection described with the system of equations described above is applied to the De Vahl Davis case [30], a differentially heated square cavity with height and width $L = 1$, shown schematically in the left graph of Figure 1. The left wall is kept at a constant temperature $T_C = -1$, while the right wall is kept at a higher constant temperature $T_H = 1$, inducing the heat transfer that drives the dynamics of the system. The top and bottom boundaries are insulated. No-slip boundary conditions for velocity are imposed on all walls.

²The limit is arbitrarily chosen and has a negligible effect on the result [12].

The difference in boundary temperatures creates a temperature gradient within the cavity that leads to natural convection. The convective flow appears due to the temperature-dependent changes in fluid density and the resulting buoyancy forces, which are described by the Boussinesq approximation term in Equation 2. The fluid cools and becomes denser at the left wall, so it falls and moves to the right, where it is heated by the hot wall, rises and completes the circular flow.

The circular flow caused by natural convection significantly increases the heat transfer between the differentially heated walls compared to conduction alone. The ratio between the two is known as the Nusselt number and provides a convenient reduction that expresses the flow dynamics in a single scalar value. Such reduction can be further analysed to determine the temporal behaviour, as shown in Figure 4, from which we can deduce when the steady state was reached. The Nusselt number used in the following analysis is calculated as the average of the values in the cold wall nodes

$$\text{Nu} = \frac{L}{T_H - T_C} \left| \frac{\partial T}{\partial x} \right|_{x=0}. \quad (5)$$

The problem is further characterised by two dimensionless numbers. The Prandtl number (Pr) is a material property that expresses the ratio between the heat and momentum transport properties of the fluid. The Rayleigh number (Ra) expresses the ratio between the strength of convective and conductive heat transport. For the purposes of this study it can be interpreted as an analogue of the Reynolds number for natural convection, with larger values implying wilder dynamics. Both Ra and Pr are a function of viscosity and must be modified to account for non-Newtonian viscosity

$$\text{Pr} = \frac{\eta_0}{\rho} \alpha^{n-2} L^{2-2n}, \quad (6)$$

$$\text{Ra} = \frac{\rho g \beta \Delta T L^{2n+1}}{\alpha^n \eta_0}, \quad (7)$$

with $\alpha = \frac{\lambda}{c_p \rho}$ as the thermal diffusivity. The definitions for the dimensionless numbers match the reference solution [13] to facilitate comparison, as does the dimensionless time

$$\hat{t} = \frac{\alpha}{H^2} t \quad (8)$$

and velocity

$$\hat{v} = \frac{L c_p \rho}{\lambda} v. \quad (9)$$

We omit the Caret notation, since dimensionless values are used wherever velocity or time are referred to in the following discussion.

3. Numerical solution procedure

Our goal is to solve the problem 1-3 using an approach that is as general as possible, including the generality of the number of dimensions, the order

of the method, and the shape of the considered domain, while supporting a spatially variable discretisation. To achieve this, we employ the RBF-FD with augmenting monomials. A meshless numerical technique operating on scattered nodes.

The first step is to discretise the domain, which in the meshless context means populating with scattered nodes. Although in the early stages of meshless development some authors used even randomly generated nodes [21], it is now generally accepted that despite the apparent robustness of meshless methods regarding the node positioning, nodes still need to be generated according to certain rules [23], i.e. nodes have to "uniformly" cover the domain with minimal empty spaces and satisfy the minimum distance requirement to avoid ill-conditioning of the approximation. There are several specially designed algorithms for meshless discretisation, ranging from expensive iterative [31] to advancing front [32] approaches. In this paper we use a Poisson disk sampling based advancing front approach [23, 33]. The core of the algorithm is the iteration, where candidate nodes are sampled around the already positioned nodes and only those that do not violate the minimal distance requirement are added to the list of discretisation nodes. This conceptually simple approach has several convenient features. It is dimensionally agnostic, meaning that the formulation of the algorithm is the same regardless of the number of dimensions of the domain. It supports variable density node distributions, which are a cornerstone of the refined solutions discussed in 4.3. It guarantees minimal spacing and is proven to be computationally efficient.

We begin the analyses with a constant density node, shown in the left panel of Figure 2), which, as we will see in section 4.3, is a wasteful strategy for the problem at hand with intense dynamics in the boundary layer as discussed in section 4.1. An improved node placement strategy, shown in the central panel of Figure 2 and discussed in 4.3, uses prior knowledge of the system to devise a refined node density that significantly reduces computational cost without sacrificing accuracy. This solution is still not ideal, as it requires physical intuition and manual input, but it demonstrates the potential for the eventual goal, which is an h -adaptive solution with appropriate error indicator. In a rightmost plot of Figure 2 we demonstrate discretisation of a an irregular domain that will be used in section 5.

Once the computational nodes are generated we identify the s nearest neighbouring nodes for each node i that form its stencil S_i . This is not a general requirement but the following description treats stencil S_i as an array of node indices sorted by distance from i -th node. As an example, the first element of stencil $S_i(1)$ is the index of the closest support node, which is almost always the i -th node itself.

In the next step we construct a generalised finite difference approximation to numerically evaluate the linear differential operator \mathcal{L} in the central node from the approximated function's values in stencil nodes

$$(\mathcal{L}u)_i \approx \sum_{j=1}^s w_{i,j} u_{S_i(j)}, \quad (10)$$

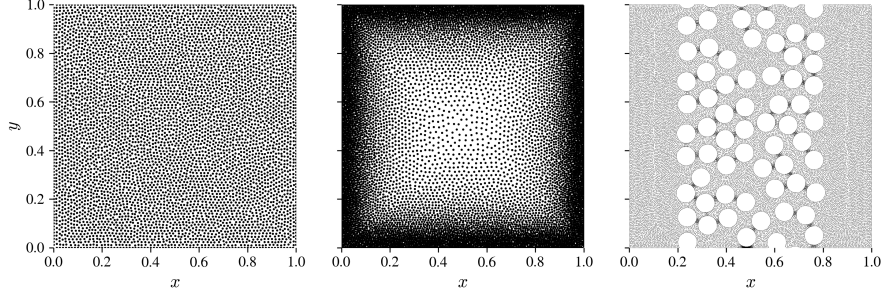


Figure 2: A comparison between node distributions in domains populated with a constant node density on the left, refined density in the middle and the obstructed domain with refined narrow channels on the right.

where u_k denotes the value of the arbitrary approximated function u at the position of the k -th node \mathbf{p}_k . The weights w are determined through the demand that the equation 10 is exact for a set of basis functions, in our case radial basis functions (RBF)

$$\phi(j, k) = \phi\left(\frac{\|\mathbf{p}_k - \mathbf{p}_j\|}{\delta_j}\right), \quad (11)$$

where we introduced δ_j as a local scaling factor that decouples the approximation from the choice of coordinate system. It is set to an arbitrary local measure of distance, e.g., the distance to the closest stencil node, and is of the utmost importance when using RBFs that use a scaling parameter. Finally, we get a local linear system $\mathbf{A}\mathbf{w}_i = \mathbf{b}$

$$\begin{bmatrix} \phi(S_i(1), S_i(1)) & \cdots & \phi(S_i(1), S_i(s)) \\ \vdots & \ddots & \vdots \\ \phi(S_i(s), S_i(1)) & \cdots & \phi(S_i(s), S_i(s)) \end{bmatrix} \begin{bmatrix} w_{i,1} \\ \vdots \\ w_{i,s} \end{bmatrix} = \begin{bmatrix} (\mathcal{L}\phi)(i, S_i(1)) \\ \vdots \\ (\mathcal{L}\phi)(i, S_i(s)) \end{bmatrix}, \quad (12)$$

for each node with the solution yielding stencil weights \mathbf{w}_i . The right hand side vector \mathbf{b} is formed by applying the linear operator \mathcal{L} to the basis function and evaluating the result with an argument analogous to equation 11.

There are multiple valid choices for basis functions. Here we use polyharmonic splines (PHS)

$$\phi(r) = r^k, \quad (13)$$

with odd order k . The main benefit of PHS RBFs is that they lack a shape parameter avoiding tedious tuning required for other popular RBF choices. Polyharmonic RBF are only conditionally positive definite and need to be augmented with monomials [34, 35]. Augmentation is additionally beneficial as it helps with reproduction of polynomials that is otherwise not generally guaranteed by RBF interpolants. The system for stencil weights is expanded with

$N_p = \binom{m+d}{m}$ monomials³ q , where m denotes the monomial order and d the spatial dimension. The monomials are scaled with a similar argumentation as RBFs in equation 11

$$q_l(j, k) = q_l \left(\frac{\mathbf{p}_k - \mathbf{p}_j}{\delta_j} \right). \quad (14)$$

The $\mathbf{A}\mathbf{w}_i = \mathbf{b}$ system for approximation weights from equation 12 is augmented with monomials

$$\begin{aligned} \begin{bmatrix} \mathbf{A} & \mathbf{Q} \\ \mathbf{Q}^T & 0 \end{bmatrix} \begin{bmatrix} \mathbf{w}_i \\ \boldsymbol{\lambda} \end{bmatrix} &= \begin{bmatrix} \mathbf{b} \\ \mathbf{c} \end{bmatrix}, \\ \mathbf{Q} &= \begin{bmatrix} q_1(S_i(1), S_i(1)) & \cdots & q_{N_p}(S_i(1), S_i(1)) \\ \vdots & \ddots & \vdots \\ q_1(S_i(s), S_i(1)) & \cdots & q_{N_p}(S_i(s), S_i(1)) \end{bmatrix}, \mathbf{c} = \begin{bmatrix} (\mathcal{L}q_1)(S_i(1), S_i(1)) \\ \vdots \\ (\mathcal{L}q_{N_p})(S_i(1), S_i(1)) \end{bmatrix}, \end{aligned} \quad (15)$$

with the additional weights $\boldsymbol{\lambda}$ treated as Lagrange multipliers and discarded after computation.

Augmentation with an order of at least $m = \frac{k-1}{2}$ is required to guarantee the positive definiteness for a PHS with order k . Higher orders provide better convergence characteristics [36] at the cost of increased computational complexity, since the required stencil size is $s \geq N_p$, with $s > 2 * N_p$ as the often recommended value [37]. Increased stencil size affects both the precomputation of the approximation weights, with complexity $\mathcal{O}((s + N_p)^3)$, and the eventual scalar product $\mathcal{O}(s)$ evaluation. We will use $k = 3$ and $m = 2$ in all numerical results presented in this paper and use s as a variable parameter. Nevertheless, augmenting monomials open an opportunity for p -adaptivity, since their order directly controls the order of the method [36, 26].

The temporal discretisation of the governing equations is solved with explicit Euler time stepping where we first update the velocity using the previous step temperature field in the Boussinesq term. The pressure-velocity coupling is performed using the Chorin's projection method under the premise that the pressure term of the Navier-Stokes equation can be treated separately from other forces and used to impose the incompressibility condition. Therefore, we express the temporal derivative with a generalised finite difference approximation to allow for explicit stepping and gather all non-pressure forces in \mathcal{F}

$$\frac{\rho}{\Delta t} (\mathbf{v}(t + \Delta t) - \mathbf{v}(t)) = -\nabla p + \mathcal{F}(\mathbf{v}(t)). \quad (16)$$

A single time step is split into two parts, the first resulting in an intermediate velocity that neglects the pressure gradient

$$\mathbf{v}^* = \mathbf{v}(t) + \frac{\Delta t}{\rho} \mathcal{F}(\mathbf{v}(t)) \quad (17)$$

³The 6 monomials in 2-D case with $m = 2$ would be $q = \{1, x, y, x^2, xy, y^2\}$.

and the second applying a pressure correction to the intermediate step

$$\mathbf{v}(t + \Delta t) = \mathbf{v}^* - \frac{\Delta t}{\rho} \nabla p. \quad (18)$$

We refer to the pressure term as correction because it does not represent the full hydrodynamic pressure. The correction pressure is calculated by solving the Poisson equation obtained by applying divergence to equation 18 and imposing equation 1 for the new velocity to ensure incompressibility

$$\cancel{\nabla \cdot \mathbf{v}(t + \Delta t)}^0 - \nabla \cdot \mathbf{v}^* = -\frac{\Delta t}{\rho} \nabla^2 p. \quad (19)$$

The new velocity is then used in the advection part of the heat transfer equation, which we solve to calculate the new temperature field.

4. Results

4.1. General flow behaviour

We will study the impact of non-Newtonian behaviour on three flow cases specified with Rayleigh and Prandtl dimensionless numbers as defined in section 2. Rayleigh numbers $\text{Ra} = \{10^4, 10^5, 10^6\}$ are chosen to capture changes in the upper range of steady natural convection regime, while $\text{Pr} = 100$ remains constant and is chosen to facilitate comparison with the existing reference solution [13]. The non-Newtonian behaviour is examined with five values for the non-Newtonian exponent $n = \{0.6, 0.7, 0.8, 0.9, 1\}$ progressing from the $n = 0.6$ case that exhibits the strongest shear-thinning behaviour to the Newtonian $n = 1$ case.

A sample of the resulting flow profiles can be seen in Figure 3 where the velocity magnitude is displayed as a heat map and overlaid with temperature contours. All cases exhibit the previously described circulation caused by natural convection, but there are drastic differences in the maximum velocity and the thickness of boundary layers as Ra and shear-thinning increase.

Both effects are expected and can be explained by the definition of varied parameters. The Rayleigh dimensionless number is defined as the product of Prandtl, which we keep constant, and Grashof dimensionless numbers. The latter expresses a ratio between buoyant and viscous forces and explains why increased Ra results in cases where fluid in the boundary layer convects away before conducting much heat to the neighbouring fluid. Similarly reduced n decreases viscous penalty for high flow velocity close to the constant temperature edges, leading to a further reduction in boundary layer thickness.

We use the Nusselt number as an observable that reduces the system's behaviour to a single scalar value that allows for temporal observation and comparison between different cases. One such example is shown in Figure 4 where we track the evolution of the Nusselt number to determine when we reach a steady state. The initial Nusselt number is high due to the high temperature gradient

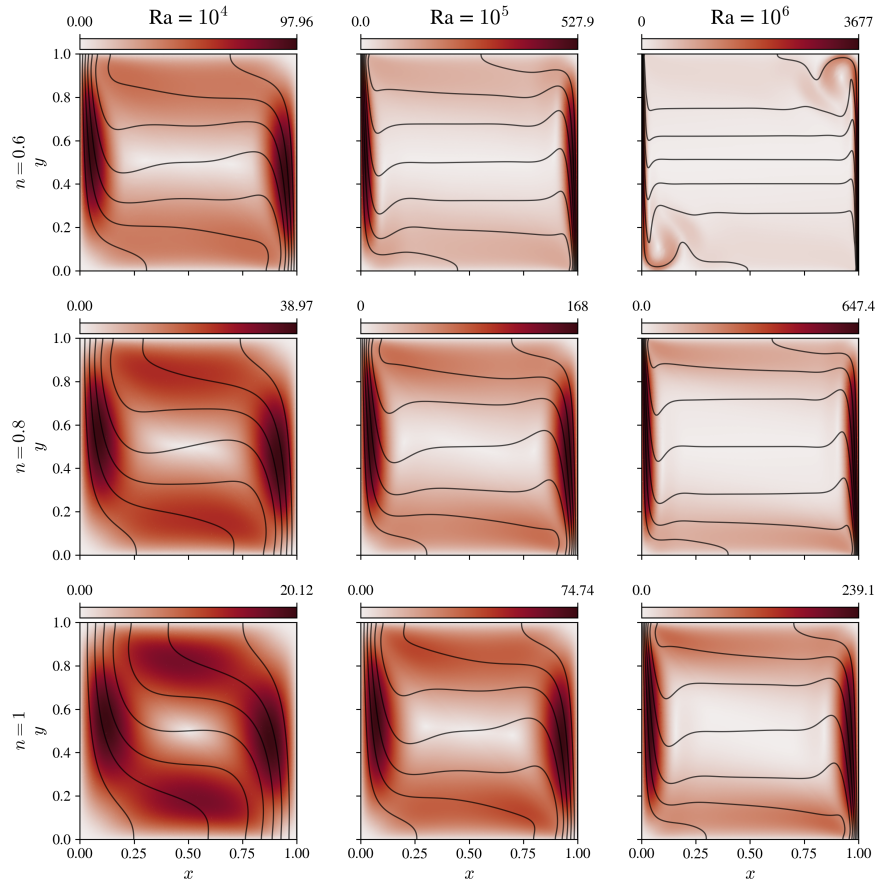


Figure 3: Flow profiles for a selection of cases. Velocity magnitude is visualised with a heatmap while the overlaid contours display the changes in temperature. Each sub-figure has a distinct velocity range specified by the colourbar above.

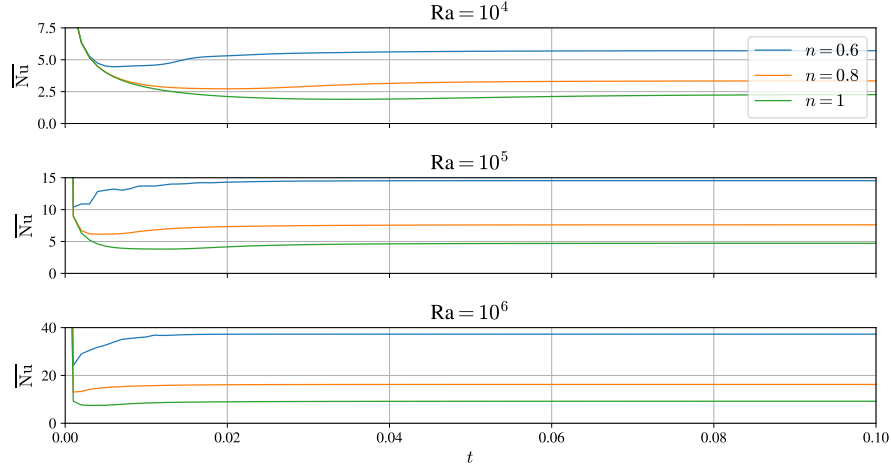


Figure 4: Time evolution of Nusselt number that is used as a scalar observable for the system’s dynamics.

at the constant temperature boundary when starting from a zero-temperature zero-velocity initial condition. The value then decreases as the importance of conductive heat transport increases until circulation is established. Using this graph, we can also observe the effects of stronger shear-thinning. Cases with lower n are faster to reach the stationary state as it is easier for convection to start with the lower effective viscosity and to play a bigger part in heat transfer as reflected in higher Nusselt values.

4.2. Convergence

The convergence analysis is performed with constant node density starting with velocity and temperature fields set to zero. End time is set to $t = 0.1$ which is determined to be sufficient to ensure that a stationary state has been reached as seen in Figure 4.

The convergence for Newtonian ($n = 1$) cases shown in the bottom row of Figure 5 is great, with even the coarsest grid providing results with less than 5% discrepancy compared to the finest. Unfortunately, this is no longer the case as we progress towards non-Newtonian cases with a thinner boundary layer. The variation of the observed values increases and the convergence rate decreases. This culminates in the most extreme case with $\text{Ra} = 10^6$ and $n = 0.6$, shown in the upper right graph of Figure 5, where adequate convergence is not achieved even though the study has already been extended to a higher node count compared to other cases. Proceeding to even higher node densities, requiring longer computational times, is wasteful, especially as the utilised numerical method allows for an elegant optimisation described in following sections.

The study was extended to include several stencil sizes in the convergence analysis. We supplemented the commonly suggested size of $2 \cdot N_p$ [37] with

$3 \cdot N_p$, $4 \cdot N_p$ and $5 \cdot N_p$, which are shown with different colours in Figure 5. The effect of increased stencil size does not appear to be significant for either the convergence rate or the final value. Based on the presented results it does not seem that increasing s beyond the recommended $2 \cdot N_p$ is worth the increased computational cost.

Furthermore, we examine the violation of symmetry

$$u(x, y) = -u(1 - x, 1 - y) \quad (20)$$

as an alternative method for assessing the fitness of the solution. First, we introduce a measure of symmetry violation by interpolating the vertical velocity v_y at an arbitrarily chosen y and $1 - y$ and calculating the relative error as

$$\epsilon = \frac{\max_{x \in [0,1]}(|v_y(x, y) + v_y(1 - x, 1 - y)|)}{\max_{x \in [0,1]}(|v_y(x, y)|)}. \quad (21)$$

where we normalise the maximum offset between a vertical velocity and its symmetric value with the maximum vertical velocity for a given case and selected y . This choice of denominator is preferable as it focuses on the symmetry errors in the relevant high velocity part of the domain while remaining relative for comparison between different cases. The resulting symmetry errors as a function of the number of nodes are shown in Figure 6 and corroborate the previous discussion that was based on convergences in Figure 5. Note that in addition to confirming the convergent behaviour of the method, the introduced symmetry violation can also be interpreted as a lower bound for the error.

There is an interesting transition in convergence curves shown in Figure 5 as we move towards upper right corner corresponding with cases that exhibit a thinner boundary layer with higher velocities. The calculated Nusselt numbers initially rise as we increase density before falling towards the value they eventually converge to. This behaviour can be better understood by examining the velocity cross-section convergence, shown in Figure 7, for the most extreme case with $\text{Ra} = 10^6$ and $n = 0.6$, where it can be seen that a certain number of nodes is required in order to adequately capture the velocity peak in the boundary layer.

4.3. Refinement

Small flow structures and large velocity gradients only occur in a relatively small part of the domain as seen in Figure 7 that covers about 5% of the domain's width and still exhibits the convective boundary layer in its entirety. Needlessly covering the entire domain with the high node density, that is only required close to the cooled and heated boundary, drastically increases the number of operations required at every time-step without improving the results.

We introduce a variable node density expressed as the distance to the nearest neighbouring node. In general, the internodal distance would be a function of position but we use a symmetric configuration, shown schematically in the left graph of Figure 8, that only depends on the distance to the closest boundary

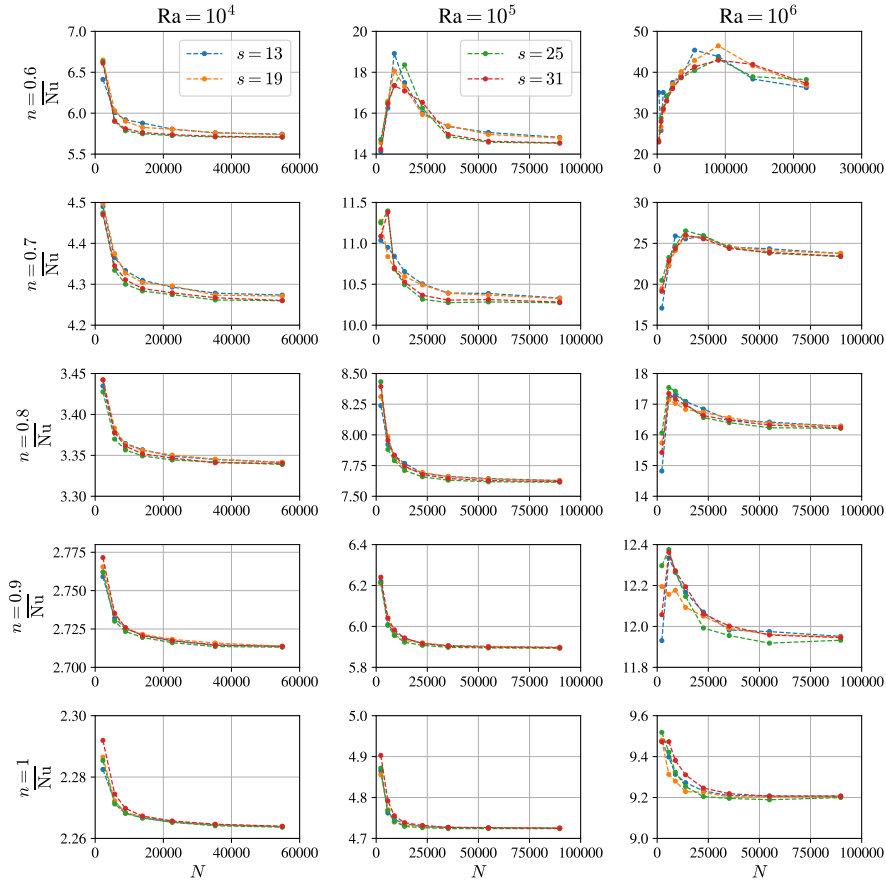


Figure 5: Convergence of the average Nusselt number on the cold boundary with columns for all of the considered Ra and rows for different non-Newtonian exponents n . The 4 considered stencil sizes s are shown with different plot colours. Node count is proportional to the internodal distance as the density is constant throughout the domain.

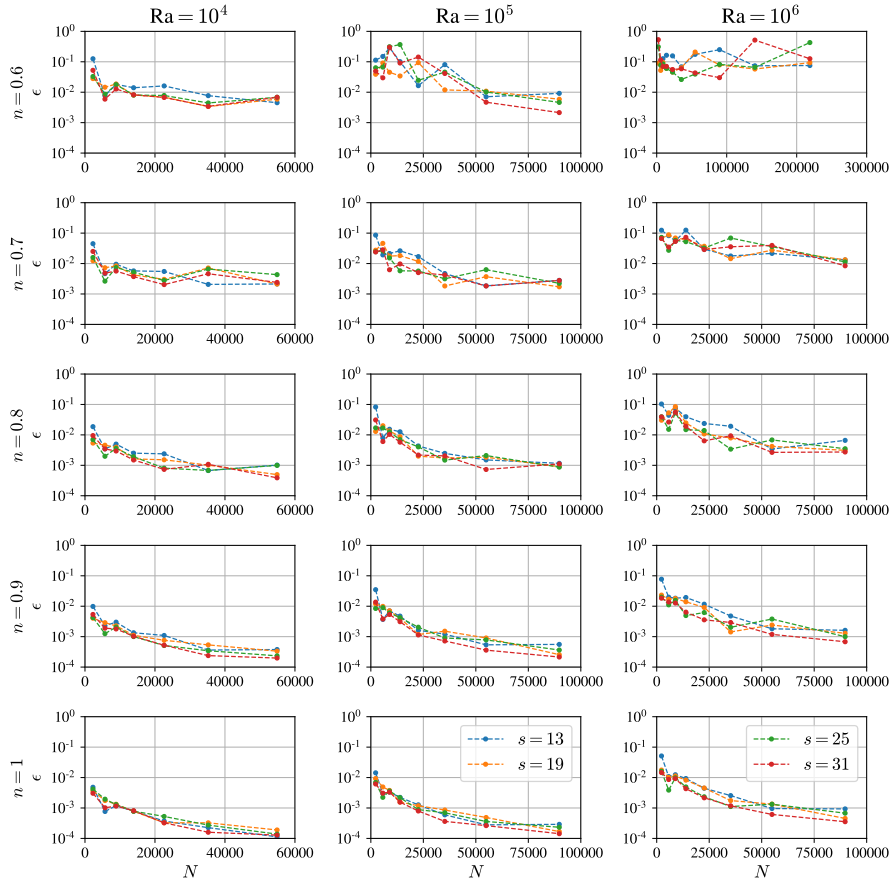


Figure 6: Convergence of the relative symmetry error at $y = 0.75$ with columns for all of the considered Ra and rows for different non-Newtonian exponents n . The 4 considered stencil sizes s are shown with different plot colours. Node count is proportional to the internodal distance as the density is constant throughout the domain.

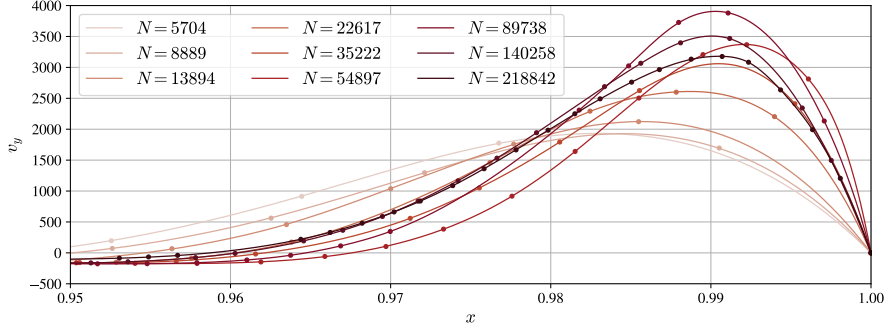


Figure 7: Convergence of interpolated vertical velocity profiles at $y = 0.6$ for the most extreme case with $\text{Ra} = 10^6$, $\text{Pr} = 100$ and $n = 0.6$. Dots display the horizontal position and vertical velocity in computational nodes that lie less than $\frac{h}{2}$ from the interpolation y .

d. The idea is to position nodes with internodal distance h_1 in a band within w of the boundary to ensure a sufficient discretisation in this intense region, while using way more coarse discretisation h_2 in the centre of the domain, with a linear transition the two

$$h = \begin{cases} h_1, & \text{where } d < w \\ h_1 + \frac{d-w}{\frac{L}{2}-w}(h_2 - h_1). & \text{otherwise} \end{cases} \quad (22)$$

This relatively simple refinement scheme leads to drastic savings in node count that rise exponentially with increasing maximum density as shown in the right graph of Figure 8. Even with the relatively conservative refinement parameters, there are almost an order of magnitude fewer nodes for low boundary internodal distances h_1 . The savings appear to be even more dramatic when a refined discretisation is visually compared to an unrefined one as seen in Figure 2.

The refinement parameters, used in Figure 8 and in other refined results with unspecified values, were chosen based on a convergence analysis. The analysis performed at $\text{Ra} = 10^6$, $\text{Pr} = 100$ and $n = 0.6$ would need to be repeated for other cases with a significant differences in boundary layer thickness and other flow characteristics. Refinement parameters have been individually varied for different border densities with the results shown in Figure 9. We assume that a further refinement in parameters would not lead to significant changes and norm the Nusselt number, shown in the upper graphs, to the best value. Normed values allow for comparison between cases with a different maximum density and conveniently show the relative offset in value.

The h_2 sweep is calculated with a band width $w = 0.05$ that is wide enough to not have a meaningful impact on the results as established in the following paragraph. The resulting Nusselt numbers, shown in the upper left graph of Figure 9, are relatively unaffected by the central internodal density h_2 , as long as it is sufficiently small to ensure numerical stability. Results are stable, with variations within 1%, until $h_2 = 0.04$ and then quickly diverge with solution

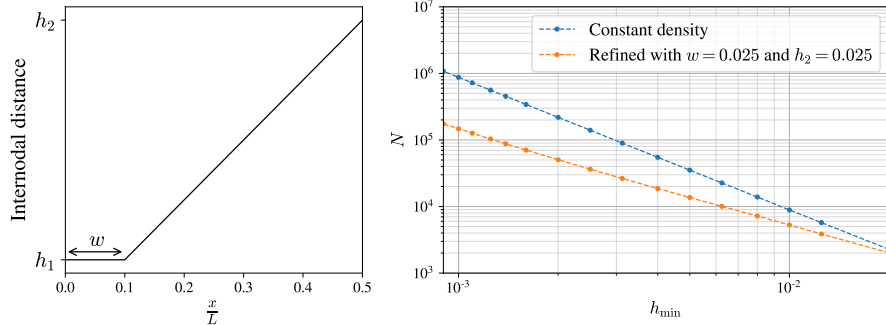


Figure 8: *left*: A schematic representation of internodal istance as a function of distance from the boundary. *right*: Computational node count as a function of minimum internodal distance for a constant density and a refined case.

procedure terminating prematurely due to numerical instability for even larger values. We chose $h_2 = 0.025$ as the optimal trade-off between the exponentially rising node count, shown in the lower left graph of Figure 9, for smaller, and a small but apparent variability at higher internodal distances.

The w sweep is calculated with a central internodal distance $h_2 = 0.02$ that has been determined to be adequate in the previous paragraph and the results are shown in the upper right graph of Figure 9. The main goal of the dense boundary band is providing a sufficient discretisation for the high velocity flow in the boundary layer. We can use Figure 7 to estimate the required width at 0.02-0.03, based on the distance from the boundary where flow velocity reduces to half its maximum value. The estimate is confirmed with numerical results that show no improvement when increasing the boundary band width w beyond a point where it covers the boundary layer flow. The effect of w is less noticeable when using smaller h_1 as the linearly decreasing density beyond the edge of the dense band still provides a sufficient density as long as the peak of the flow is covered. We chose $w = 0.025$ as the refinement parameter for further use as it provides the same results as $w = 0.1$, especially at smaller h_1 that we are mainly interested in, while providing a significant reduction in node count as seen from the lower right graph of Figure 9.

The symmetric refinement approach is not ideal, but is suitable as a proof-of-concept due to the small number of density function parameters, which simplifies their analysis and selection. A simple improvement would be to treat the non-insulated and insulated boundaries differently, since the latter do not exhibit the sharp convective flow layer and can be discretised with a lower density. The real improvements to refinement can become arbitrarily complex and focus on deriving an error indicator based either on a previous, less refined solution or on the properties of the numerical method itself.

We use the refined density to recalculate the convergence for $\text{Ra} = 10^6$, $n = 0.6$ case that did not converge with the constant density discretisations. The

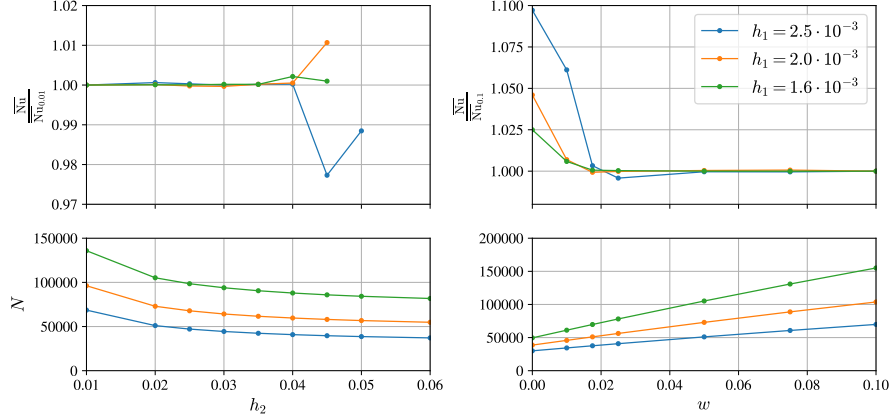


Figure 9: Impact of refinement scheme parameter variation on the Nusselt number show in the top and node count in the bottom graphs. Nusselt values are normed to the value attained with the best considered parameter value. *left*: Variation of the central internodal distance h_2 with the dense boundary band held constant at $w = 0.05$. *right*: Variation of the dense boundary band w with the central node spacing held constant at $h_2 = 0.02$.

initial values for velocity and temperature fields are interpolated from the best previously obtained results in order to shorten the simulation time required to reach a stationary state. The new convergence results are shown in Figure 10 for two different stencil sizes s . Not only is convergence achieved, but it is also achieved with a significantly smaller number of nodes and with a drastically reduced symmetry error.

4.4. Comparison with reference data

Non-Newtonian fluid dynamics in a differentially heated cavity have already been tackled previously, and we have performed our study on a matching case for verification. We use the results provided by Turan et al. [13] and Kim et al. [12], who used FVM with SIMPLE coupling and Upwind or QUICK stabilisation. We compare those results with a refined RBF-FD and Chorin projection, without stabilisation of convective terms to minimise the effect of numerical diffusion.

Both publications provide an empirical fit for the average Nusselt number as a function of Rayleigh number Ra , Prandtl number Pr and non-Newtonian

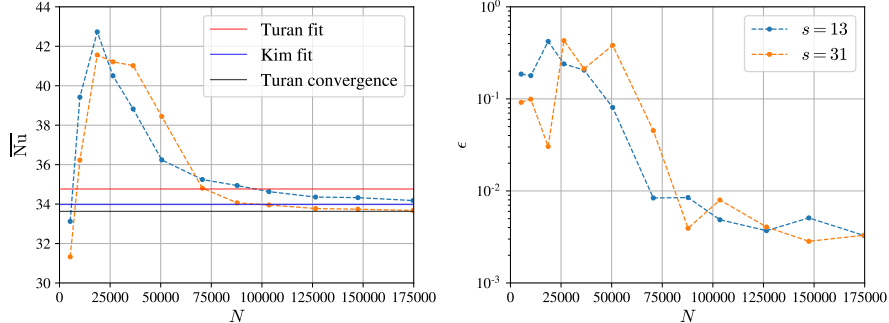


Figure 10: *left*: Convergence study for the problematic $\text{Ra} = 10^6$, $n = 0.6$ case repeated with a refined density. Red and blue horizontal lines show Nusselt values derived from correlations defined in equations 24 and 25 while the black shows the best value from the convergence study presented in Turan et al. [13]. *right*: The relative symmetry error for the repeated convergence study.

exponent n

$$\overline{\text{Nu}}_{\text{Turan}} = 0.162 \text{Ra}^{0.043} \frac{\text{Pr}^{0.341}}{(1 + \text{Pr})^{0.091}} \left(\frac{\text{Ra}^{(2-n)}}{\text{Pr}^n} \right)^{\frac{1}{2(n+1)}} \exp(C(n-1)), \quad (23)$$

$$C = \begin{cases} 1.343 \text{Ra}^{0.065} \text{Pr}^{0.036} & \text{where } n \leq 1 \\ 0.858 \text{Ra}^{0.071} \text{Pr}^{0.034} & \text{otherwise} \end{cases}, \quad (24)$$

$$\overline{\text{Nu}}_{\text{Kim}} = 0.3n^{0.4} \text{Ra}^{\frac{1}{3n+1}}, \quad (25)$$

that we can use to compare against our results.

The Nusselt values calculated by the provided correlations are added to Figure 10, supplemented by the exact numerical value from the convergence study performed by Turan et al. on this case. All results agree well, with small deviations that are normal due to discretisation errors and different numerical methods. We must also keep in mind that the provided correlations, in all their complexity, are still only empirical fits over a wide range of flow regimes and suffer accordingly, as can be seen from the large discrepancy between the Turan fit and the convergence value from the corresponding study.

We extend the fit comparison to all cases considered with the results shown in Figure 11. All computed values fall within the range of the provided correlation functions, again confirming that the meshless RBF-FD method yields valid results. The relative difference between the fits increases significantly for calmer cases with a smaller Nusselt number, casting further doubt on the accuracy of the empirical fits for a wide range of parameters. The case-dependent discrepancy between our numerical results and the provided fits is similar to that in the source publication.

We also tested different stencil sizes for all cases. The difference between the results computed with different stencils is in all cases smaller than the difference

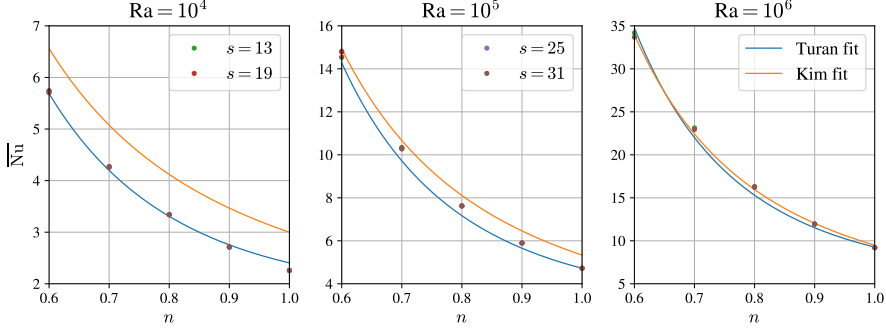


Figure 11: Comparison between the calculated Nusselt values and correlations provided in existing literature. Solid lines represent correlations defined in equations 24 and 25.

between Turan et al. and Kim et al. which means that the small stencil $s = 13$ suffices for a stable and accurate computation. Using more nodes in stencil results only leads to a wasteful number crunching.

We report the average Nusselt value at the cold boundary calculated with the finest discretisation for the full range of considered parameters at $\text{Pr} = 100$ in Table 1.

Ra	$n = 0.6$	$n = 0.7$	$n = 0.8$	$n = 0.9$	$n = 1$
10^4	5.71	4.26	3.34	2.71	2.26
10^5	14.55	10.28	7.62	5.90	4.72
10^6	33.68	22.95	16.24	11.95	9.21

Table 1: A table of the best obtained average Nusselt values for all of the considered parameters. Presented values are calculated with $s = 5$. Refined density used for the problematic $\text{Ra} = 10^6$, $n \in \{0.6, 0.7\}$ cases.

5. Geometrical flexibility

Finally, we apply the described solution procedure to more complex domains in order to demonstrate the geometrical flexibility that we touted as one of the main benefits. In the first example, shown in Figure 12 we add circular obstructions to the central part of the De Vahl Davis case to simulate how the non-Newtonian behaviour would impact the convective flow passing through a porous filter. The computational node distribution used in this case, shown in the right panel of Figure 2, utilises a modified refinement strategy that increases node density in narrow channels and on nearby boundaries to ensure that at least two computational nodes discretise the channel's width. Even though the dimensionless numbers defined in section 2 are no longer suitable for this case we stick with them to enable comparison with flow profiles shown in Figure 3. We

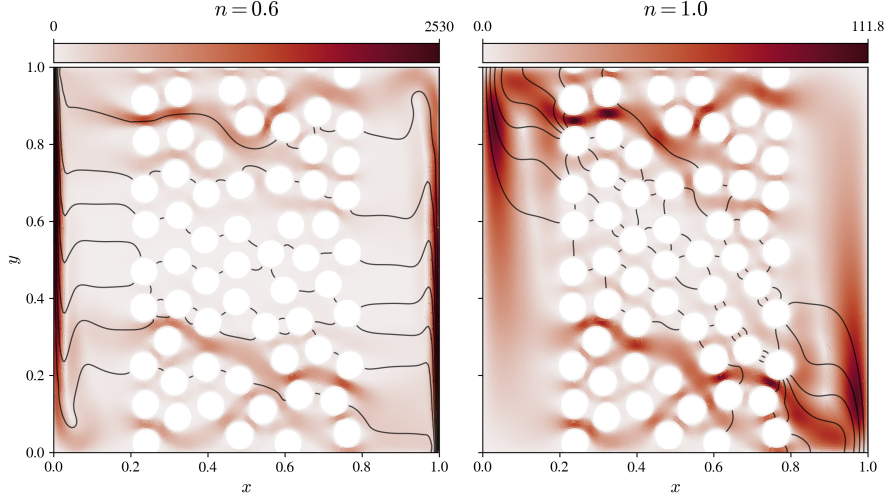


Figure 12: Flow profiles for $\text{Ra} = 10^6$, $\text{Pr} = 100$ case with a porous central section. Velocity magnitude is visualised with a heat-map while the overlaid contours display the changes in temperature. The strongest shear-thinning $n = 0.6$ case is shown on the left sub-figure while the right displays the Newtonian $n = 1.0$ case.

use the same random filter configuration for the shear-thinning non-Newtonian fluid on the left and the Newtonian fluid on the right graph. The results are unsurprising with both the change in temperature profile and the reduction of maximum velocity confirming that the filter's narrow channels present a far greater hindrance for the Newtonian fluid.

The shear-thinning filter case presents a suitable opportunity to examine the spatial variation in viscosity shown in Figure 13. We show the inverse of viscosity to better highlight the shear-thinning aspect with the most affected areas corresponding to edges of the high velocity layer next to the vertical walls and in high velocity channels through the filter as seen in Figure 12. Viscosity behaviour next to the vertical walls is identical to the non filter cases.

We formulated the method in a dimensionally agnostic manner, which can be with some effort directly transformed into dimensionally agnostic object-oriented code design [38], using powerful C++ template systems. The filtered 2D case can thus be quickly transformed into its 3D variant shown in Figure 14 with minimal interference in the core code that is limited only to the parameters (refer to the supplied repository for the actual code). For better visual representation plane intersections of the vertical velocity, temperature and viscosity are presented in Figure 15. The purpose of presenting this 3D results is twofold. First, we want to demonstrate the ability of the presented method to address a complex physical problem on an irregular 3D domain. Second, we want to demonstrate the powerful concept of merging the generally formulated RBF-FD

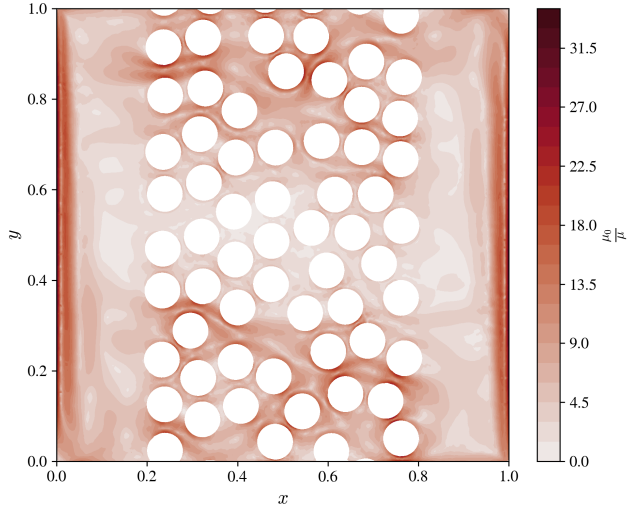


Figure 13: Variation in viscosity due to shear-thinning effects. Higher values signify lower viscosity due to the normed inverse visualisation that is chosen to highlight the areas where shear rate caused thinning is the strongest.

method with a generic programming to design an dimension independent solution procedure. More details on the C++ implementation aspect can be found in [38].

6. Conclusions

In this paper, we have proposed a dimension independent refined meshless solution procedure for NNC. The main advantage of the proposed approach is that it can operate on scattered nodes, which greatly facilitates the consideration of complex 3D domains and the implementation of refinement, both of which are demonstrated in this paper. Moreover, the approximation weights are computed individually, allowing for a variation in the stencil size s , monomial augmentation order m , the type and order of the RBFs used, etc. Even the method used to construct the generalised finite differences can be changed, e.g. to the least squares radial basis function finite difference method [39]. The ease of adaptation on all mentioned levels allows the use of a sophisticated but slow approximation only where it is truly needed with faster alternatives elsewhere, which is often the majority of the domain when dealing with realistic cases.

From the non-Newtonian fluid dynamics point of view, we presented new results for the benchmark case that is already solved with two similar FVM approaches [13, 12] with a fundamentally different numerical approach and, most

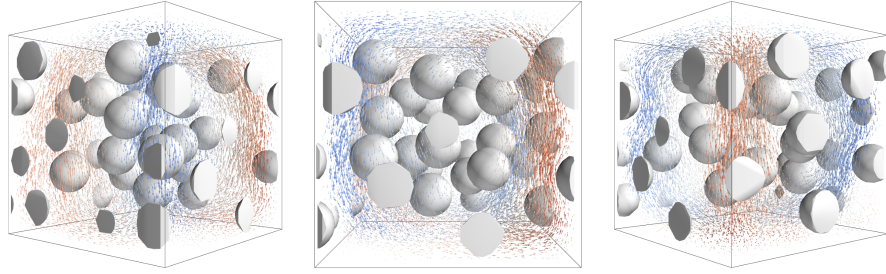


Figure 14: Natural convection in a 3D differentially heated cavity with obstructions. This case differs from the previous as the temperature differential and resulting flow is now vertical.

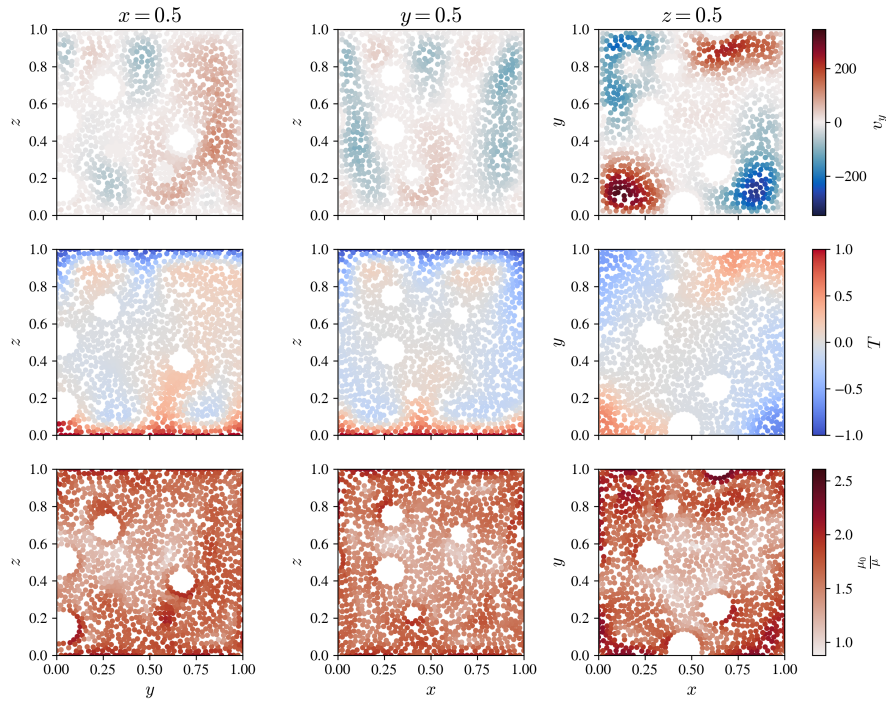


Figure 15: Plane intersections of the 3D case shown in Figure 14. The first row displays vertical velocity, the second row the temperature and the third row the inverse of the shear-thinning viscosity. Values and positions shown on the scatter plot correspond to computational nodes within $\frac{h}{2}$ of the intersecting plane.

importantly, without stabilisation that effectively introduce numerical diffusion in the solution.

In future work, we will consider implementation of an h-adaptive solution, which requires an adequate error indicator and a refinement logic that constructs the target node density function from the error indicator data and refines the nodes accordingly [25]. Furthermore, we plan to implement an hp-adaptive approach [26], where we need an additional step to determine the optimal order of the method [36]. In addition, we also plan to analyse how hyperviscosity [40] and adaptive upwind [41] stabilisations, and using different approximation approaches [42] affects the flow structures.

7. Acknowledgements

The authors would like to acknowledge the financial support of the Slovenian Research Agency (ARRS) research core funding No. P2-0095 and the Young Researcher program PR-10468.

References

- [1] A. Rahimi, A. D. Saee, A. Kasaeipoor, E. H. Malekshah, A comprehensive review on natural convection flow and heat transfer: the most practical geometries for engineering applications, *International Journal of Numerical Methods for Heat & Fluid Flow* (2018).
- [2] A. Bejan, *Convection heat transfer*, John Wiley & Sons, 2013. doi:10.1002/9781118671627.
- [3] R. P. Chhabra, *Non-Newtonian Fluids: An Introduction*, Springer New York, New York, NY, 2010, pp. 3–34.
URL https://doi.org/10.1007/978-1-4419-6494-6_1
- [4] X. Wang, X. Li, Numerical simulation of three dimensional non-newtonian free surface flows in injection molding using ale finite element method, *Finite Elements in Analysis and Design* 46 (7) (2010) 551 – 562. doi: <https://doi.org/10.1016/j.finel.2010.02.003>.
- [5] S. Charm, G. Kurland, Viscometry of human blood for shear rates of 0–100,000 sec⁻¹, *Nature* 206 (4984) (1965) 617–618. doi:10.1038/206617a0.
- [6] A. Gratão, V. Silveira, J. Telis-Romero, Laminar flow of soursop juice through concentric annuli: Friction factors and rheology, *Journal of Food Engineering* 78 (4) (2007) 1343 – 1354. doi:<https://doi.org/10.1016/j.jfoodeng.2006.01.006>.
- [7] J. Welti-Chanes, F. Vergara-Balderas, D. Bermúdez-Aguirre, Transport phenomena in food engineering: basic concepts and advances, *Journal of Food Engineering* 67 (1) (2005) 113 – 128, iV Iberoamerican Congress of Food Engineering (CIBIA IV). doi:<https://doi.org/10.1016/j.jfoodeng.2004.05.053>.

- [8] E. C. Bingham, An investigation of the laws of plastic flow, no. 278, US Government Printing Office, 1917.
- [9] L. Yang, K. Du, A comprehensive review on the natural, forced, and mixed convection of non-newtonian fluids (nanofluids) inside different cavities, *Journal of Thermal Analysis and Calorimetry* (2019) 1–22doi:10.1007/s10973-019-08987-y.
- [10] J. Kwack, A. Masud, A stabilized mixed finite element method for shear-rate dependent non-newtonian fluids: 3D benchmark problems and application to blood flow in bifurcating arteries, *Computational Mechanics* 53 (4) (2014) 751–776. doi:10.1007/s00466-013-0928-6.
URL <https://doi.org/10.1007/s00466-013-0928-6>
- [11] S. Patankar, Numerical heat transfer and fluid flow, taylor & francis london (1980).
- [12] G. B. Kim, J. M. Hyun, H. S. Kwak, Transient buoyant convection of a power-law non-newtonian fluid in an enclosure, *International Journal of Heat and Mass Transfer* 46 (19) (2003) 3605–3617. doi:10.1016/s0017-9310(03)00149-2.
- [13] O. Turan, A. Sachdeva, N. Chakraborty, R. J. Poole, Laminar natural convection of power-law fluids in a square enclosure with differentially heated side walls subjected to constant temperatures, *Journal of Non-Newtonian Fluid Mechanics* 166 (17-18) (2011) 1049–1063. doi:10.1016/j.jnnfm.2011.06.003.
- [14] M. V. Bozorg, M. Siavashi, Two-phase mixed convection heat transfer and entropy generation analysis of a non-newtonian nanofluid inside a cavity with internal rotating heater and cooler, *International Journal of Mechanical Sciences* 151 (2019) 842–857.
- [15] N. O. Moraga, M. A. Marambio, R. C. Cabrales, Geometric multigrid technique for solving heat convection-diffusion and phase change problems, *International Communications in Heat and Mass Transfer* 88 (2017) 108–119. doi:10.1016/j.icheatmasstransfer.2017.08.012.
- [16] D. A. Vasco, N. O. Moraga, G. Haase, Parallel finite volume method simulation of three-dimensional fluid flow and convective heat transfer for viscoplastic non-newtonian fluids, *Numerical Heat Transfer, Part A: Applications* 66 (9) (2014) 990–1019.
- [17] D. S. Loenko, A. Shenoy, M. A. Sheremet, Natural convection of non-newtonian power-law fluid in a square cavity with a heat-generating element, *Energies* 12 (11) (2019) 2149. doi:10.3390/en12112149.
- [18] A. Alsabery, A. Chamkha, H. Saleh, I. Hashim, Transient natural convective heat transfer in a trapezoidal cavity filled with non-newtonian

nanofluid with sinusoidal boundary conditions on both sidewalls, *Powder Technology* 308 (2017) 214–234.

- [19] L. Mishra, R. P. Chhabra, Natural convection in power-law fluids in a square enclosure from two differentially heated horizontal cylinders, *Heat Transfer Engineering* 39 (10) (2018) 819–842.
- [20] G. R. Kefayati, Simulation of magnetic field effect on natural convection of non-newtonian power-law fluids in a sinusoidal heated cavity using fdlbm, *International Communications in Heat and Mass Transfer* 53 (2014) 139–153.
- [21] G.-R. Liu, Mesh free methods: moving beyond the finite element method, CRC press, 2002. doi:10.1201/9781420040586.
- [22] A. I. Tolstykh, D. A. Shirobokov, On using radial basis functions in a “finite difference mode” with applications to elasticity problems, *Computational Mechanics* 33 (1) (2003) 68–79. doi:10.1007/s00466-003-0501-9.
- [23] J. Slak, G. Kosec, On generation of node distributions for meshless PDE discretizations, *SIAM Journal on Scientific Computing* 41 (5) (2019) A3202–A3229. doi:10.1137/18M1231456.
- [24] A. J. Chorin, Numerical solution of the navier-stokes equations, *Mathematics of computation* 22 (104) (1968) 745–762.
- [25] J. Slak, G. Kosec, Adaptive radial basis function-generated finite differences method for contact problems, *International Journal for Numerical Methods in Engineering* 119 (7) (2019) 661–686.
- [26] M. Jančič, J. Slak, G. Kosec, p-refined rbf-fd solution of a poisson problem, in: 2021 6th International Conference on Smart and Sustainable Technologies (SpliTech), IEEE, 2021, pp. 01–06.
- [27] Gitlab repository, https://gitlab.com/e62Lab/public/2022_p-refinednonnewtonianconvection.
- [28] J. D. Anderson Jr, Fundamentals of aerodynamics, Tata McGraw-Hill Education, 2010.
- [29] D. J. Tritton, Physical Fluid Dynamics, Oxford Science Publ, Clarendon Press, 1988. doi:https://doi.org/10.1007/978-94-009-9992-3.
- [30] G. De Vahl Davis, Natural convection of air in a square cavity: A bench mark numerical solution, *International Journal for Numerical Methods in Fluids* 3 (3) (1983) 249–264. doi:https://doi.org/10.1002/fld.1650030305.
- [31] D. P. Hardin, E. B. Saff, Discretizing manifolds via minimum energy points, *Notices of the AMS* 51 (10) (2004) 1186–1194.

- [32] V. Shankar, R. M. Kirby, A. L. Fogelson, Robust node generation for mesh-free discretizations on irregular domains and surfaces, *SIAM J. Sci. Comput.* 40 (4) (2018) 2584–2608. [doi:10.1137/17m114090x](https://doi.org/10.1137/17m114090x).
- [33] M. Depolli, J. Slak, G. Kosec, Parallel domain discretization algorithm for rbf-fd and other meshless numerical methods for solving pdes (2022). [arXiv:2202.01457](https://arxiv.org/abs/2202.01457).
- [34] N. Flyer, B. Fornberg, V. Bayona, G. A. Barnett, On the role of polynomials in rbf-fd approximations: I. interpolation and accuracy, *Journal of Computational Physics* 321 (2016) 21–38. [doi:<https://doi.org/10.1016/j.jcp.2016.05.026>](https://doi.org/10.1016/j.jcp.2016.05.026).
- [35] J. Slak, Adaptive rbf-fd method, Ph.D. thesis, University of Ljubljana (2020).
URL <https://repozitorij.uni-lj.si/IzpisGradiva.php?lang=eng&id=121511>
- [36] M. Jančič, J. Slak, G. Kosec, Monomial augmentation guidelines for rbf-fd from accuracy versus computational time perspective, *Journal of Scientific Computing* 87 (1) (2021) 9. [doi:10.1007/s10915-020-01401-y](https://doi.org/10.1007/s10915-020-01401-y).
- [37] N. Flyer, G. A. Barnett, L. J. Wicker, Enhancing finite differences with radial basis functions: Experiments on the navier–stokes equations, *Journal of Computational Physics* 316 (2016) 39 – 62. [doi:<https://doi.org/10.1016/j.jcp.2016.02.078>](https://doi.org/10.1016/j.jcp.2016.02.078).
- [38] J. Slak, G. Kosec, Medusa: A c++ library for solving pdes using strong form mesh-free methods, *ACM Trans. Math. Softw.* 47 (3) (Jun. 2021). [doi:10.1145/3450966](https://doi.org/10.1145/3450966).
- [39] I. Tominec, E. Larsson, A. Heryudono, A least squares radial basis function finite difference method with improved stability properties, *SIAM Journal on Scientific Computing* 43 (2) (2021) A1441–A1471.
- [40] V. Shankar, A. L. Fogelson, Hyperviscosity-based stabilization for radial basis function-finite difference (rbf-fd) discretizations of advection–diffusion equations, *Journal of Computational Physics* 372 (2018) 616 – 639. [doi:<https://doi.org/10.1016/j.jcp.2018.06.036>](https://doi.org/10.1016/j.jcp.2018.06.036).
- [41] G. Kosec, B. Šarler, Simulation of macrosegregation with mesosegregates in binary metallic casts by a meshless method, *Engineering analysis with boundary elements* 45 (2014) 36–44.
- [42] V. Hatič, B. Mavrič, B. Šarler, Meshless simulation of a lid-driven cavity problem with a non-newtonian fluid, *Engineering Analysis with Boundary Elements* 131 (2021) 86–99.